Applied Catalysis B: Environmental 148–149 (2014) 36–43

Contents lists available at ScienceDirect

Applied Catalysis B: Environmental

journal homepage: www.elsevier.com/locate/apcatb

Ag/CeO_2 nanospheres: Efficient catalysts for formaldehyde oxidation

Lei Ma[a,b], Dingsheng Wang[a,*], Junhua Li[b,*], Bingyang Bai[b], Lixin Fu[b], Yadong Li[a]

[a] Department of Chemistry, Tsinghua University, Beijing 100084, China
[b] State Key Joint Laboratory of Environment Simulation and Pollution Control, School of Environment, Tsinghua University, Beijing 100084, China

ARTICLE INFO

Article history:
Received 28 June 2013
Received in revised form 9 September 2013
Accepted 18 October 2013
Available online 27 October 2013

Keywords:
Formaldehyde (HCHO)
Complete catalytic oxidation
Ag/CeO_2
Surface oxygen activation
Formate

ABSTRACT

Ag/CeO_2 nanosphere catalysts, prepared by a one-step hydrothermal method, were used to eliminate the indoor formaldehyde (HCHO) pollution. The activity test results showed that Ag/CeO_2 nanosphere catalysts exhibited much higher catalytic activity than normal Ag/CeO_2 particles prepared by conventional impregnation method. Ag/CeO_2 nanosphere catalysts could reach complete HCHO oxidation above 110 °C under relatively high space velocity. The specific reaction rate per second and per unit of surface area of Ag/CeO_2 nanosphere catalysts were almost 3.6 times higher than normal Ag/CeO_2 particle catalysts at 110 °C. The prepared catalysts were also characterized by various methods. HRTEM, BET, and XRD results showed that Ag/CeO_2 products were nanosphere shapes with average sizes around 80–100 nm, and were comprised of many small particles with a crystallite size of 2–5 nm. Cerium and silver were well distributed throughout the individual Ag/CeO_2 nanosphere crystal. According to the results in XPS, H_2-TPR, O_2-TPD, and Raman spectra, surface chemisorbed oxygen easily formed on the Ag/CeO_2 nanosphere catalysts. The synergetic interaction might exist between Ag and CeO_2 nanosphere, and the presence of silver could facilitate surface chemisorbed oxygen activation, which mainly contributed to the HCHO oxidation. Based on In-situ DRIFTS results, formate species ($HCOO^-$) were found to be the key intermediates and be activated on the surface active oxygen of Ag/CeO_2 nanosphere catalysts in the catalytic oxidation process of HCHO, which would be further oxidized into the final product water and carbon dioxides.

1. Introduction

Formaldehyde (HCHO) is one of the major pollutants for indoor air pollution, which becomes an incentive of a variety of diseases. Formaldehyde can cause watery eyes, burning sensations in the eyes and throat, nausea, and difficulty in breathing in some humans exposed at elevated levels. Thus, it is very important for reducing the indoor HCHO emission to achieve the stringent emission regulation.

It is recognized that catalytic oxidation technology is an effective way to eliminate the formaldehyde pollutants [1]. Many kinds of catalysts, including transition metal oxide and precious metal catalysts, have been reported to be active for complete catalytic oxidation technology of formaldehyde elimination. For example, Transition metal oxide catalysts included MnO_2 [2], Cr_2O_3 [3], Co_3O_4 [4,5], and Co–Mn oxide [6]. Meanwhile, the precious metals, including Pt [7], Pd [8], and Au [9] show much application potentials for HCHO oxidation. Especially, Au/CeO_2 catalysts have received much attention for catalytic oxidation reaction of HCHO in recent years [10–15]. It was reported that complete oxidation of HCHO could be obtained on Au/CeO_2 at 80 °C [10]. Furthermore, Zhang et al. [12] successfully developed good distribution of catalytic Au nanoparticles with the three-dimensionally ordered macroporous structures, which would exhibit complete HCHO conversion at approximately 75 °C. Zhu et al. [15] further improved preparation method of Au/CeO_2 catalysts, and found that Au/CeO_2 prepared by deposition–precipitation method could achieve complete HCHO conversion into CO_2 and H_2O at room temperature, even in the wet air under high space velocity. Overall, the high catalytic activity of Au/CeO_2 catalysts was mainly related to the surface area, highly dispersed Au species, the coexistence of active species Au^{3+} and Au^0, and weak adsorption of CO_2 [11,13,14].

On the basis of present research, some of the catalysts based on precious metals could achieve complete catalytic oxidation of HCHO, such as Au/CeO_2 [15], Pt/TiO_2 [16], Pt/MnO_x-CeO_2 [17]. However, with the price of precious metals continuing to increase, it is still a challenge for developing low cost catalysts. It was reported that Ag nanoparticles or supported Ag catalysts exhibited some remarkable ability in the catalytic oxidation reaction including HCHO oxidation [18–22]. Therefore, Ag should be a good choice for catalytic oxidation of HCHO.

Due to remarkable oxygen storage ability, CeO_2 have attracted much attention and been served as a catalyst support material [23]. Thus, Ag/CeO_2 was considered as one of the effective catalysts for catalytic oxidation reaction, and could achieve almost

* Corresponding author. Tel.: +86 1062773422.
E-mail addresses: wangdingsheng@mail.tsinghua.edu.cn (D. Wang), lijunhua@tsinghua.edu.cn (J. Li).

0926-3373/$ – see front matter © 2013 Elsevier B.V. All rights reserved.
http://dx.doi.org/10.1016/j.apcatb.2013.10.039

complete oxidation of HCHO above 200 °C by Imamura et al. [24], who found that silver–cerium composite oxide could contribute to highly active oxidation of HCHO. The high activity was ascribed to the high silver dispersion and surface oxygen activation. Meanwhile, compared to CeO_2 catalyst, Ag/CeO_2 catalyst preferred to produce much more deeply oxidized species, which would be easily removed and transformed to final water and CO_2. Furthermore, Mao and Vannice [25] thought that the formate groups were the major key organic intermediates for HCHO oxidation on Ag/Al_2O_3, which would be further oxidized on Ag surface. A certain amount of dioxymethylene species also existed and could be transformed into formate species.

It is well known that nano particles have very strong size effects and electronic effects for catalytic reaction, and have been studied extensively in the past decades [26]. Ag/CeO_2 catalysts might be the promising catalyst for HCHO oxidation, and could achieve highly efficient HCHO removal at low temperature through the adjustment and control of catalyst structure. In this work, we developed serial CeO_2 and Ag/CeO_2 nanosphere catalysts based on our previous work [27]. The results showed that the HCHO oxidation ability was significantly improved on Ag/CeO_2 nanosphere catalysts compared to normal Ag/CeO_2 particle catalyst. The serial CeO_2 and Ag/CeO_2 catalysts were also characterized in detail, and the possible reaction mechanism for HCHO oxidation on Ag/CeO_2 nanosphere catalysts were proposed based on In-situ DRIFTS experiments.

2. Experimental

2.1. Preparation of Catalysts

The CeO_2 nanospheres were synthesized by hydrothermal method reported previously [27]. In a typical synthesis process, 1.0 g of $Ce(NO_3)_3{\cdot}6H_2O$ was dissolved in 1 mL of deionized water. Then, 1 mL of propionic acid and 30 mL of glycol were added with stirring to form a uniform solution. The mixed solution was sealed and heated at 180 °C for 240 min to get the products. Furthermore, Ag/CeO_2 nanospheres were prepared that a certain amount of $AgNO_3$ (AR) was added and dispersed in the mixed solution in the process of CeO_2 nanosphere preparation. After intense stirring for several minutes, the mixture was sealed and heated at 180 °C for 240 min to get the products. After the hydrothermal treatment, the mixture was filtered and washed several times with ethanol. The obtained solid was dried at 110 °C overnight. The obtained catalysts are denoted as Ag/CeO_2-N, CeO_2-N, respectively.

Meanwhile, the CeO_2 and Ag/CeO_2 bulk particles were prepared for comparison. CeO_2 was prepared by the thermal decomposition of $Ce(NO_3)_3{\cdot}6H_2O$ at 550 °C under air for 4 h, and denoted as CeO_2-P. The Ag/CeO_2 was prepared by a wet impregnation method with $AgNO_3$ (AR) precursors and denoted as Ag/CeO_2-P.

Finally, all of the prepared catalysts were calcined at 300 °C for 4 h for further evaluation and characterization. The Ag contents on both Ag/CeO_2–N and Ag/CeO_2–P were approximately 2 wt%. The surface element contents of the prepared samples were characterized by X-ray photoelectron spectroscopy (XPS), while the chemical compositions were determined by inductively coupled plasma optical emission spectroscopy (ICP-OES) with an IRIS Intrepid II XSP apparatus from Thermo Fisher Scientific Inc. The related results were summarized in Table 1.

2.2. Activity test of catalyst

Catalytic activity tests were performed in a fixed-bed quartz tube reactor of 9 mm internal diameter containing 50 mg of catalyst powder mixed with quartz sand. In the tests, a flowing N_2 mixture containing 810 ppm HCHO and 20% O_2 was introduced into the reactor. Formaldehyde gas was generated by an incubator kept at 30 °C, in which N_2 was injected through a washing bottle filled with formalin solution (an aqueous solution of 37% HCHO). The total flow rate was fixed at 100 mL/min, which corresponded to a GHSV (gas hourly space velocity) of 84,000 h^{-1}. The concentration of HCHO in the inlet and outlet gas was measured by an online gas chromatograph of Agilent 7890A equipped with FID and TCD detectors. To avoid the impact of gas adsorption on the catalyst samples, the test data were recorded after the reactions had maintained stable states.

The performance of the catalysts is presented in terms of conversion of HCHO (X(HCHO)) as defined:

$$X(\mathrm{HCHO}) = \frac{[\mathrm{CO_2}]_{\mathrm{outlet}}}{[\mathrm{HCHO}]_{\mathrm{inlet}}} \times 100\%$$

The $[HCHO]_{inlet}$ and $[CO_2]_{outlet}$ in the formula are the HCHO concentration in the gas flow and the CO_2 concentration in the products, respectively.

2.3. Characterization of catalyst

Transmission electron microscope (TEM) was performed on a Hitachi HT7700 with an acceleration voltage of 100 kV. High-resolution transmission electron microscope (HRTEM) was performed on a FEI Tecnai G^2 F20 S-TWIN with an acceleration voltage of 200 kV. The powder X-ray diffraction (XRD) measurements were carried out with a D8 advance system with Cu $K\alpha$ radiation.

A Quantachrome Nova Automated Gas Sorption System was used to measure the N_2 adsorption isotherms of the samples at the temperature of liquid N_2 (−196 °C). The specific surface area was determined from the linear portion of the BET plot. The pore size distribution was calculated from the desorption branch of the N_2 adsorption isotherm using the BJH method. Prior to the surface area and pore size distribution measurements, the samples were degassed under vacuum at 300 °C for 4 h.

The X-ray photoelectron spectroscopy (XPS) experiment was carried out on a PHI Quantera SXM system at room temperature under 3.1×10^{-8} Pa using Al^+ radiation. Binding energy of all the elements was calibrated relative to the carbon impurity with a C 1s at 284.8 eV.

Hydrogen temperature programmed reduction (H_2-TPR) and oxygen temperature programmed reduction (O_2-TPD) experiments were performed on a Micromeritics ChemiSorb 2720 apparatus. In each experiment, 100 mg of sample was loaded into a quartz reactor and then pretreated in N_2 (50 mL/min) at 300 °C for 1 h. The sample was then cooled to room temperature under a stream of N_2. For H_2-TPR experiment, the reduction process was carried out from room temperature to 1000 °C under a flow of 10% H_2/Ar (50 mL/min) at 10 °C/min. For O_2-TPD experiment, the adsorption of O_2 was carried out in a flow of 5% O_2/He for 30 min (50 mL/min), and then purged by He for 30 min for removal of residual oxygen. The catalyst was then heated to 1000 °C in a flow of He (50 mL/min) at 10 °C/min. The consumption of H_2 or O_2 was continuously monitored with a thermal conductivity detector.

Raman spectra were measured by Microscopic Confocal Raman Spectrometer (Renishaw, RM2000) under ambient conditions using a laser with wavelength of 532 nm. The spectra were recorded with a resolution of 1 cm^{-1} and a scan number of 20 from 40 to 1300 cm^{-1}.

The In-situ DRIFTS experiments were recorded with a Nicolet Nexus spectrometer equipped with a liquid nitrogen-cooled MCT detector. Praying Mantis™ High Temperature Reaction Chamber from Harrick Scientific Products Inc. were used as the environmental chamber, while a dome with two KBr windows and one glass observation window were used on the chamber. The samples were placed onto a sample cell within an atmospherically controllable

Table 1
XPS and ICP-OES analysis of the chemical compositions of different CeO_2 and Ag/CeO_2 catalysts.

Catalysts	XPS					ICP-OES		
	Ag (at%)	Ce (at%)	O (at%)	O/Ag (at/at)	Ag/Ce (at/at)	Ag (wt%)	Ce (wt%)	Ag/Ce (at/at)
CeO_2-P		72.7	27.3					
Ag/CeO_2-P	2.5	71.6	25.9	10.36	0.03	2.3	76.4	0.04
CeO_2-N		72.7	27.3					
Ag/CeO_2-N	1.8	74.6	23.6	13.11	0.02	2.6	74.9	0.05

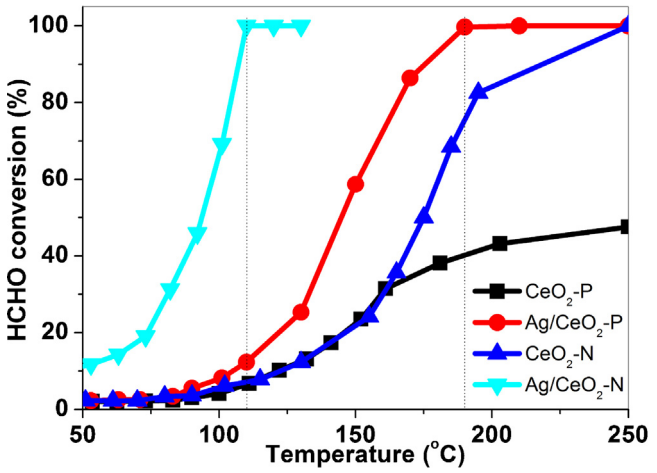

Fig. 1. The performance of catalytic oxidation of HCHO on different CeO_2 and Ag/CeO_2 catalysts. Reaction conditions: 50 mg catalyst, 810 ppm HCHO, 20% O_2, and balance N_2, GHSV = 84,000 h^{-1}.

chamber for DRIFTS spectroscopic analysis. A circulating water kept the outside of the chamber cool when operating at high temperatures. In the experiment, the samples were purged in a flow of 20% O_2/N_2 at 200 °C for 30 min, and then cooled to 25 °C. The IR spectra were recorded by accumulating 100 scans at a spectral resolution of 4 cm^{-1}. The gas mixtures were the same as the activity test (ambient conditions).

3. Results and discussion

3.1. Catalytic oxidation performance of different catalysts

Fig. 1 shows the catalytic activity of HCHO oxidation on different CeO_2 and Ag/CeO_2 catalysts. It can be seen that maximum HCHO conversion of the serial catalysts ranks in the sequence of Ag/CeO_2-N > Ag/CeO_2-P > CeO_2-N > CeO_2-P in the whole temperature range. The HCHO conversions of CeO_2-P are lower than 50% in a wide temperature range, which is very similar to previous study in which CeO_2 particles were not very effective for HCHO oxidation [24]. Yet, the catalytic activity of Ag/CeO_2-P is slightly improved and reaches 100% at 190 °C. In comparison, the CeO_2-N catalysts show relatively higher catalytic activity than CeO_2-P, and reach HCHO conversion of 50% at 175 °C and maximum HCHO conversion of approximately 100% at 250 °C. When the Ag nano particles are doped onto CeO_2-N support, surprisingly high HCHO conversions are gotten and reach approximately 100% conversion at 110 °C.

In addition, to eliminate the influence of the surface area, specific reaction rate (R_s) in term of consumed amount of HCHO per second and per unit of surface area is also calculated and given in Table 2. It shows that the R_s of Ag/CeO_2-N catalyst is 8.8 nmol/s/m^2 and almost 3.6 times higher than Ag/CeO_2-P catalyst regardless of larger surface area of Ag/CeO_2-N. This result indicates that the HCHO oxidation is significantly improved on the Ag/CeO_2-N nanosphere catalysts. For comparison, we calculate the corresponding R_s of the catalysts at the temperature when complete HCHO oxidation took place in previous study. Results shows that R_s was 0.7 nmol/s/m^2 on Au/Co_3O_4–CeO_2 [28], 1.6 nmol/s/m^2 on Ag/MnO_x-CeO_2 [18], 3.2 nmol/s/m^2 on Ag-HMO [21], and 0.3 nmol/s/m^2 on Pt/f-SiO_2 [29], respectively. Meanwhile, turn over frequency (TOF) was also calculated based on the total silver content and compared with related research results. The TOF of Ag/CeO_2-N is 0.005 s^{-1} at 110 °C in comparison to a corresponding value of 0.004 s^{-1} for HCHO oxidation at 220 °C on Ag/SiO_2 catalyst [25]. Overall, Ag/CeO_2 nanospheres have relatively higher specific reaction rate and TOF at 110 °C implying that they should be potential catalysts for HCHO oxidation.

3.2. Characterization of the catalysts

3.2.1. Crystal and structural properties

Transmission electron microscopy (TEM) images show that both of CeO_2 and Ag/CeO_2 products are the nanosphere shapes with average sizes around 80–100 nm (Fig. 2a and b). Furthermore, CeO_2-P particle size is obviously larger than CeO_2 nanospheres, and has the irregular shape with the size of approximately 3.2 μm (figure not given). In addition, the Ag/CeO_2-N crystallite size is estimated by the HRTEM results (Fig. 2c), in which the Ag/CeO_2-N nanospheres are comprised of many small particles with a crystallite size of 2–5 nm, and there are clear voids among the small particles. The corresponding elemental maps of Ag/CeO_2-N nanospheres show that both Ce and Ag are well distributed throughout the individual Ag/CeO_2 nanosphere crystal (Fig. 2d). The *d* lattice spacing is 0.312 nm, while FFT results indicate that the Ag/CeO_2 nanosphere crystals mainly exposure (1 1 1) planes of fluorite structure of CeO_2 (Fig. 2e).

BET surface area and pore volume results are summarized in Table 2. The surface area and pore volume of the CeO_2-P catalysts are 57.8 m^2/g and 0.024 cm^3/g, respectively. For Ag/CeO_2-P catalysts, they decrease to 55.5 m^2/g and 0.023 cm^3/g indicating that the introduction of silver slightly decreases the CeO_2 particle surface area. It can be speculated that the physical structure of Ag/CeO_2-P catalysts would not change with silver doping due to the similar pore structure values between the impregnated Ag/CeO_2-P catalysts and CeO_2-P supports. In addition, the nanostructure obviously gives much higher surface area and pore volume. The surface area and pore volume of CeO_2-N are 148.6 m^2/g and 0.063 cm^3/g, while the corresponding value of Ag/CeO_2-N are 125.4 m^2/g and 0.054 cm^3/g, respectively. For Ag/CeO_2-N catalysts, surface area and pore volume decrease somewhat, indicating that silver nano particles formed on the surface with blocking pores of CeO_2 nanospheres.

Fig. 3 shows the XRD pattern of the different CeO_2 and Ag/CeO_2 catalysts. The intensive diffraction peaks of CeO_2-P are observed at 2θ = 28.6, 33.1, 47.5, 56.3, 59.1, 69.4, 76.7, 79.1, and 88.4°, which can be attributed to the (1 1 1), (2 0 0), (2 2 0), (3 1 1), (2 2 2), (4 0 0), (3 3 1), (4 2 0), and (4 2 2) plane diffraction of the fluorite structure of CeO_2 (JCPDS 34-0394). While CeO_2-N catalysts show similar diffraction peaks as the CeO_2-P catalysts, however the diffraction peaks obviously become broader than CeO_2-P catalysts, demonstrating the formation of nanostructures of CeO_2. Compared to the diffraction pattern of CeO_2-P, two additional weak diffraction peaks

Table 2
Textural properties, crystallite sizes, lattice parameters, and specific reaction rate (R_s) of different CeO_2 and Ag/CeO_2 catalysts.

Catalysts	BET (m^2/g)	Pore volume (cm^3/g)	Crystallite sizes of CeO_2 (nm)	Lattice parameters (nm)	R_s ($nmol/s/m^2$)[a]
CeO_2-P	57.8	0.024	17.4	0.5403	1.3
Ag/CeO_2-P	55.5	0.023	14.8	0.5405	2.4
CeO_2-N	148.6	0.063	2.5	0.5410	0.5
Ag/CeO_2-N	125.4	0.054	2.4	0.5411	8.8

[a] Reaction conditions: catalyst = 50 mg, HCHO = 810 ppm, O_2 = 20%, and N_2 balance, gas rate = 100 mL/min, and temperature = 110 °C.

at 2θ of 38.2° and 44.4° are detected on Ag/CeO_2-P catalysts, which could be attributed to the (1 1 1) and (2 0 0) Bragg's reflections of the face-centered cubic (fcc) structure of Ag (JCPDS 65-2871) [30,31]. Note that, the diffraction peaks at 2θ of 38.1° could be also the (2 0 0) Bragg's reflections of body-centered cubic (bcc) structure of Ag_2O (JCPDS 65-6811). Therefore, it is difficult to exclude the presence of Ag_2O on the Ag/CeO_2-P catalysts [31]. The following H_2-TPR study might further demonstrate this speculation. For Ag/CeO_2-N catalysts, there were more total silver contents according to the ICP-OES results in Table 1, and the diffraction peaks are almost the same as that of CeO_2-N. Thus, no obvious Ag or Ag_2O is observed in the XRD pattern except fluorite structure of CeO_2 implying that silver nano particles well disperse on the CeO_2-N supports. As shown in Table 2, the detailed analysis of the XRD patterns using JADE 5.0 software gives crystallite sizes and lattice parameters of the different samples. The results showed that the crystallite sizes of CeO_2 obviously decreased on the CeO_2 and Ag/CeO_2 nanosphere catalysts, which resulted in the larger surface area and pore volume. Compared to CeO_2-P and CeO_2-N catalysts, the lattice parameters slightly increased on Ag/CeO_2-P and Ag/CeO_2-N catalysts, respectively. This might indicate some incorporation of Ag^+ cations into CeO_2 lattice because the ionic radius of Ag^+ is larger than that of Ce^{4+}.

3.2.2. Active surface oxygen

To investigate the chemical states of oxygen on prepared samples, O1s measured by XPS are deconvoluted to obtain detailed information of the surface species, and are summarized in Fig. 4. The O 1s XPS data shows a peak around 529.3 eV with a shoulder around 531.3 eV. The common main peaks at 529.3 eV might be ascribed to lattice oxygen (O_{lat}), and the peak at 531.3 eV could be attributed to surface chemisorbed oxygen (O_{sur}). From the data observed, CeO_2-P and Ag/CeO_2-P mainly exhibit lattice oxygen and some amount of surface chemisorbed oxygen, while the surface ratio of $O_{sur}/(O_{sur}+O_{lat})$ is approximately 51% and 52%, respectively. The CeO_2-N and Ag/CeO_2-N catalysts show a relatively higher surface chemisorbed oxygen, and the ratio of $O_{sur}/(O_{sur}+O_{lat})$ are 56% and 61%, respectively. In addition, the O/Ag atomic ratio of Ag/CeO_2-N was calculated by the surface element compositions in XPS results (Table 1), and this value exceeded the corresponding value of Ag/CeO_2-P. This should be due to the existence of abundant surface oxygen species on Ag/CeO_2 nanosphere catalysts. The much

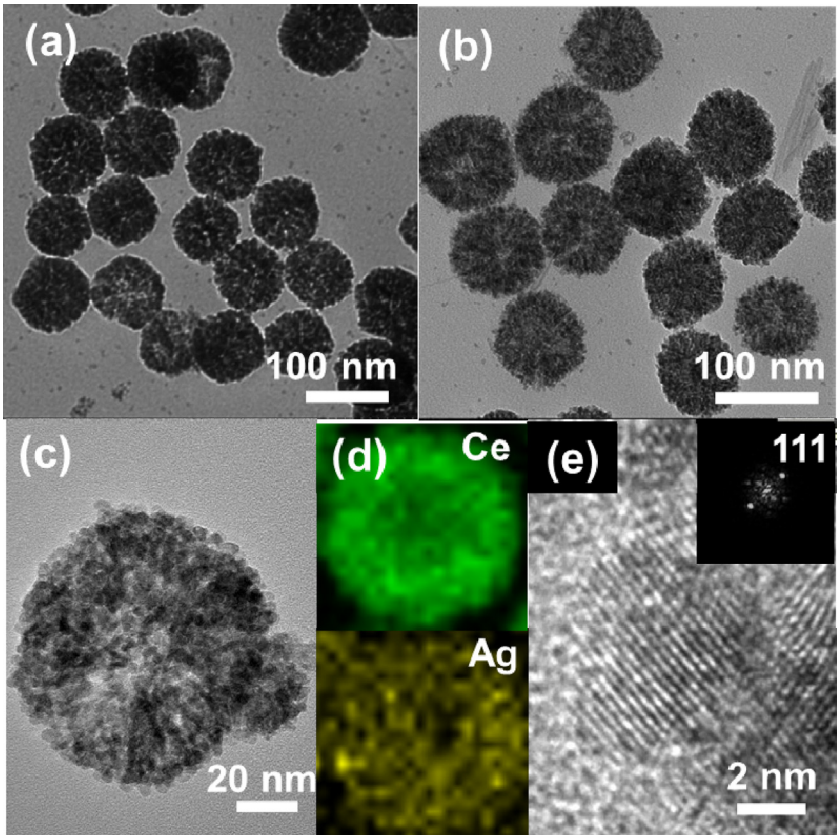

Fig. 2. (a) TEM image of the CeO_2-N nanosphere, (b) TEM image of Ag/CeO_2-N nanosphere, (c) HRTEM images of Ag/CeO_2-N nanosphere, (d) The distribution of element maps of Ce (green) and Ag (yellow) on Ag/CeO_2-N nanosphere, and (e) HRTEM image of the Ag/CeO_2-N nanosphere (Top-right inset show the corresponding FFT pattern). (For interpretation of the references to color in this figure legend, the reader is referred to the web version of this article.)

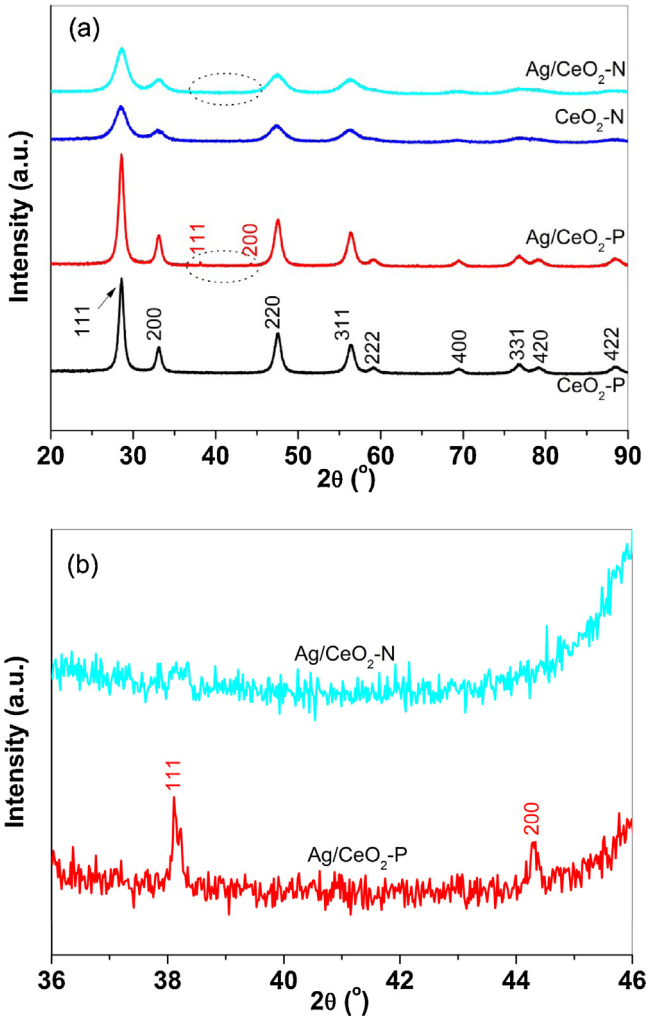

Fig. 3. XRD pattern of different CeO_2 and Ag/CeO_2 catalysts.

surface chemisorbed oxygen might be beneficial to activate the HCHO molecules that facilitated the catalytic oxidation reaction.

In addition, Fig. 5 shows the Ag3d XPS spectra of the Ag/CeO_2 catalysts. The $Ag3d_{5/2}$ binding energy of Ag/CeO_2-P catalysts is 368.3 eV, which could be attributed to the Ag^0 of the metal Ag. Meanwhile, the binding energy of Ag/CeO_2-N catalysts slightly shifts to lower value of 368.0 eV indicating the formation of oxidation state of silver nano particles on the surface of Ag/CeO_2-N

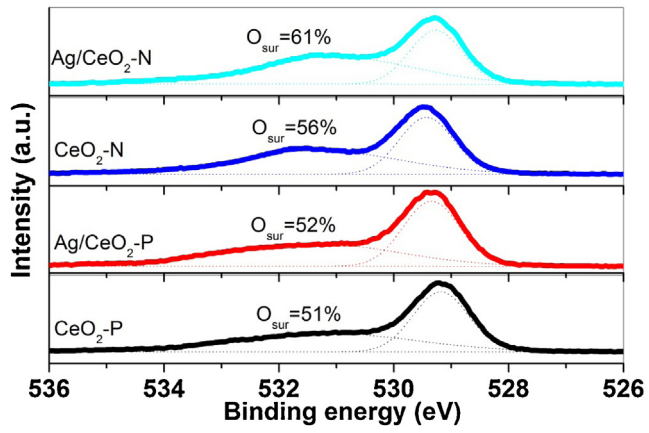

Fig. 4. O1s XPS of different CeO_2 and Ag/CeO_2 catalysts.

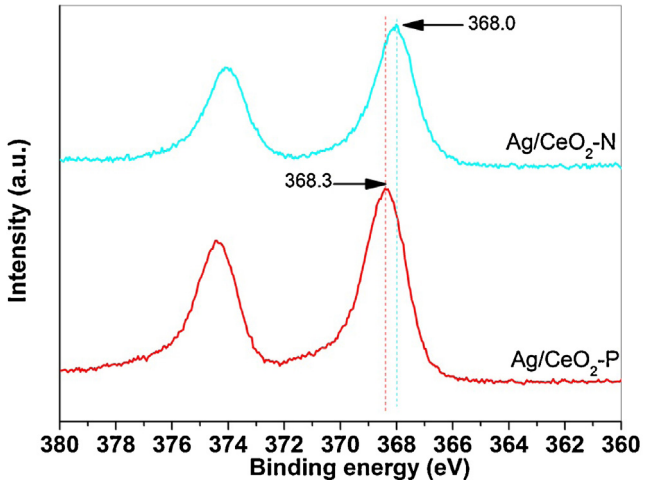

Fig. 5. Ag3d XPS of different Ag/CeO_2-P and Ag/CeO_2-N catalysts.

catalysts. Since the binding energy for Ag^+ of Ag_2O is always around 367.6–367.8 eV [32,33]. Therefore, we speculate that parts of the Ag nano particles are oxidized, and both metallic Ag and Ag_2O are formed on Ag/CeO_2-N catalyst surface. It should be mentioned that the surface Ag/Ce atomic ratio of Ag/CeO_2-P catalysts was slightly less than that of the bulk, while the surface Ag/Ce atomic ratio of Ag/CeO_2-N catalysts was much less than that of the bulk (Table 1). This indicated that the silver species mainly existed in the bulk phase for both of the Ag/CeO_2-P and Ag/CeO_2-N catalysts. Especially, the major part of silver well dispersed in bulk phase of the Ag/CeO_2-N catalysts rather than the surface.

Fig. 6 shows H_2-TPR profiles of different CeO_2 and Ag/CeO_2 catalysts. In the temperature region 50–900 °C, CeO_2-P catalysts show three reduction peak located at 411, 527 and 813 °C, respectively. The two reduction peaks at low temperatures could be attributed to reduction of surface active oxygen (such as O^{2-} and O^-) of ceria while the one peak at high temperature could be reduction of lattice oxygen of bulk CeO_2 [14]. Ag/CeO_2-P catalysts show an intense reduction peak centered at 203 °C and a broad peak at 813 °C while there are almost no reduction peaks between 411 and 527 °C. As shown in Fig. 6, the hydrogen consumption of the reduction peak at 203 °C is calculated, while the theoretical value of hydrogen consumption on Ag/CeO_2 is also calculated based on the assumption of Ag_2O formation from Ag concentration in ICP-OES results

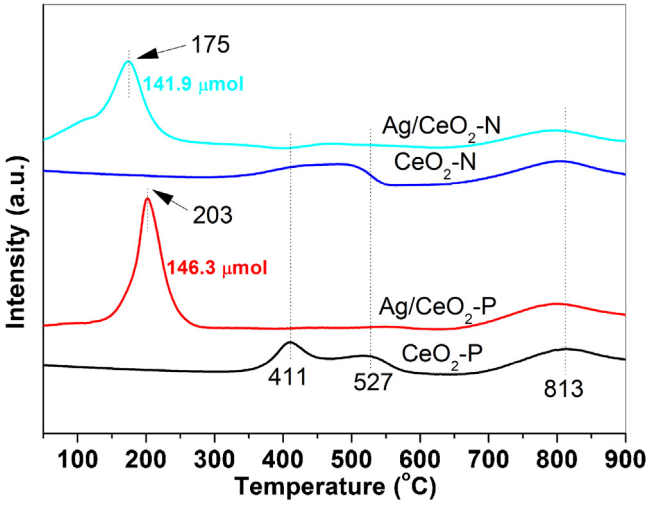

Fig. 6. H_2-TPR profiles of different CeO_2 and Ag/CeO_2 catalysts.

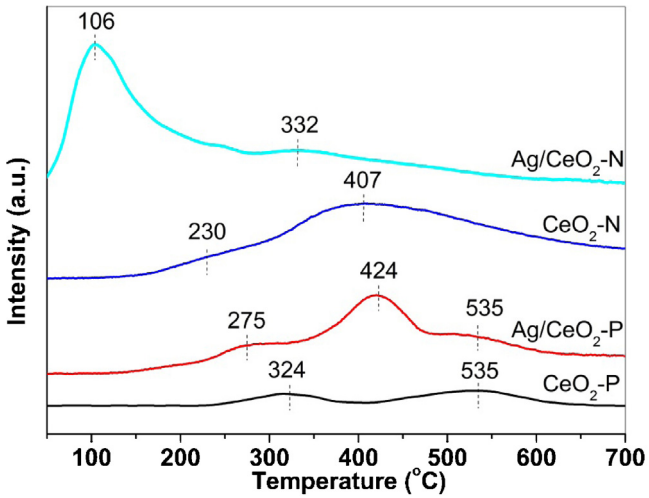

Fig. 7. O_2-TPD profiles of different CeO_2 and Ag/CeO_2 catalysts.

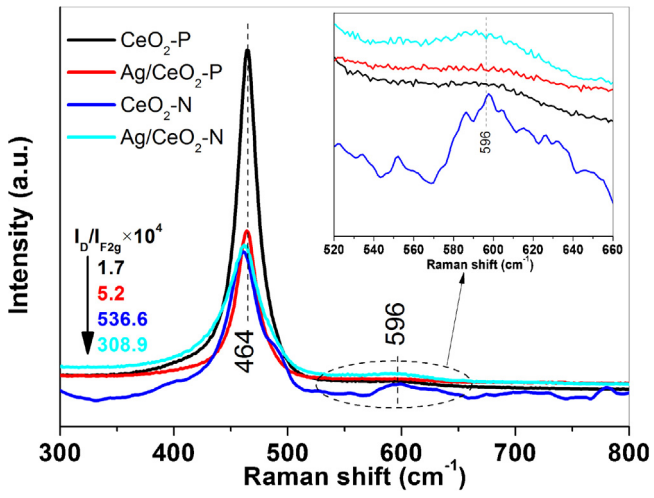

Fig. 8. Raman spectra of different CeO_2 and Ag/CeO_2 catalysts at room temperature.

(Table 1). Results indicate that the actual hydrogen consumption of 146.3 μmol is much higher than the theoretical value of 10.7 μmol. Therefore, the hydrogen consumption amount of Ag/CeO_2-P at 203 °C is much higher than the corresponding peaks of CeO_2-P, suggesting this reduction peak involved oxygen from both silver and ceria oxides. This is consistent with the previous report that the presence of silver could improve the reducibility of surface oxygen on CeO_2 and facilitated the oxygen transfer during the reduction process [31,34]. Therefore, the two reduction peaks of Ag/CeO_2-P at low and high temperatures could be attributed to the reduction peaks of surface active oxygen of ceria interacting with silver and the bulk oxygen of ceria, respectively. In addition, the H_2-TPR profiles of CeO_2-N show similar hydrogen reduction peaks as the CeO_2-P. Meanwhile, there are two hydrogen reduction peaks on Ag/CeO_2-N catalysts, where the first hydrogen reduction peak obviously shifts to low temperature, while the second one is almost stable at 813 °C. Similarly, the actual H_2 consumption of Ag/CeO_2-N at 175 °C is 141.9 μmol, which is also higher than the theoretical value of 9.3 μmol, indicating the reduction process of surface active oxygen from silver and ceria at low temperature. Compared to the reduction profiles of Ag/CeO_2-P, the binding energy of the Ag-O and Ce-O for the Ag/CeO_2-N nanosphere catalysts is most likely weakened, while the presence of silver nano particles would obviously facilitate the reduction process in the H_2-TPR test.

Fig. 7 shows O_2-TPD profiles of different CeO_2 and Ag/CeO_2 catalysts. It was reported that the surface active oxygen species such as O^{2-} and O^- desorbed around 300 °C, whereas lattice oxygen from CeO_2 would desorb at relatively higher temperature [28]. Therefore, the oxygen desorption peaks of CeO_2-P catalysts at 324 and 535 °C could be assigned to surface active oxygen species and lattice oxygen desorption, respectively. Because desorption of oxygen from surface active oxygen species located at 106 °C on Ag/CeO_2-N, 230 °C on CeO_2-N, 275 °C on Ag/CeO_2-P, and 324 °C on CeO_2-P, the activity of surface active oxygen for catalytic oxidation reaction on four catalysts should rank in the sequence of Ag/CeO_2-N > CeO_2-N > Ag/CeO_2-P > CeO_2-P. Furthermore, on the basis of O_2-TPD peak area, the total oxygen desorption amount ranked as Ag/CeO_2-N > Ag/CeO_2-P and CeO_2-N > CeO_2-P, respectively. These results imply that Ag/CeO_2 and CeO_2 catalysts with nanosphere structures would facilitate to generate much more oxygen desorption during temperature programmed process.

Raman spectra of different CeO_2 and Ag/CeO_2 catalysts are summarized and given in Fig. 8. Serial CeO_2 and Ag/CeO_2 catalysts show two Raman adsorption peaks, one intense peak located at 464 cm^{-1} and one weak peak at 596 cm^{-1}. These two peaks could be attributed to the strong F_{2g} vibration mode of fluorite structure and defect-induced (D) mode, respectively [35]. The relative intensity ratio of I_D/I_{F2g}, inserted into the plot in Fig. 8 is related to the oxygen defect sites of the catalysts, which followed the sequence CeO_2-N > Ag/CeO_2-N ≫ Ag/CeO_2-P > CeO_2-P. These results indicate that the CeO_2-N and Ag/CeO_2-N nanospheres have much more intrinsic defect sites in fluorite structure. Compared to CeO_2-P, the generation of oxygen vacancies on Ag/CeO_2-P might be ascribed the incorporation of Ag into the lattice of ceria oxides [31].

In general, CeO_2 nanosphere catalysts consisted of many small nanoparticles, and also contained much more defects especially surface oxygen by nano size effect. The abundant oxygen vacancies could adsorb and activate O_2 for facilitating the catalytic oxidation reaction [13]. More importantly, silver species well dispersed, and only showed very small crystallites on Ag/CeO_2 nanosphere catalysts. The presence of silver nano particles promoted desorption of surface active oxygen on Ag/CeO_2-N catalysts. Compared to other catalysts, Ag/CeO_2-N catalysts would easily desorb surface active oxygen species and exhibit higher catalytic activity for formaldehyde oxidation. Thus, it should be speculated that both of the nano CeO_2 and Ag crystallites contributed to the enhanced activity for HCHO oxidation reaction.

3.2.3. *Possible reaction intermediates*

To demonstrate intermediate species and reaction mechanism for HCHO oxidation, In-situ DRIFTS were recorded as a function of time after 810 ppm HCHO + 20% O_2/N_2 was introduced into the cell at 70 °C. Transient reaction results (Figs. S1 and S2) show that formate species ($HCOO^-$, around 1580 cm^{-1}) and C–H bands (around 2740, 2850, and 2930 cm^{-1}) mainly form on series of CeO_2 and Ag/CeO_2 catalysts. The negative bands with absorbance appeared at around 3650 cm^{-1} during exposure to HCHO could be interpreted that the formation of formate results in the consumption of surface hydroxyls groups (O–H bands).

At 70 °C, two bands due to weakly adsorbed C–H bands (around 2850 and 2930 cm^{-1}), and strongly adsorbed formate (around 1580 cm^{-1}) species are detected on Ag/CeO_2-N catalyst, when it is treated in flowing $HCHO/N_2$ or $HCHO + O_2/N_2$. After it is purged by the N_2 for another 30 min, the peaks of C–H and formate do not obviously decrease, yet surface hydroxyls decrease at the meantime. Further purging treatment by O_2/N_2 would not affect the C–H, formate, and surface hydroxyls adspecies. In contrast, the process of HCHO adsorption followed by purging with N_2 will slightly decrease the surface adsorbed C–H and formate species on CeO_2-P and CeO_2-N catalysts. Therefore, it seems that

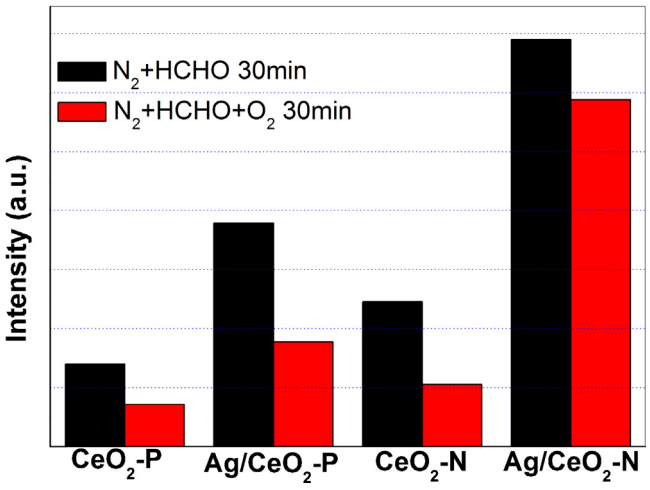

Fig. 9. Formation of $HCOO^-$ (indicated by band area around 1580 cm^{-1}) at 70 °C upon passing 810 ppm HCHO + 20% O_2/N_2 over different CeO_2 and Ag/CeO_2 catalysts.

the presence of silver will stabilize the $HCOO^-$ species on the Ag/CeO_2 catalysts. Moreover, for these four catalysts, there are different features of $HCOO^-$ adsorption between HCHO adsorption and HCHO + O_2 adsorption, while the HCHO adsorption process significantly improved much more $HCOO^-$ formation than that of the HCHO + O_2 adsorption process.

The bands around 1580 cm^{-1}, represented $HCOO^-$ generation, are formed after HCHO is introduced on the CeO_2 and Ag/CeO_2 catalysts. Research results indicated that $HCOO^-$ might be a key intermediate species in the HCHO oxidation reaction [16,24,25]. Fig. 9 summarizes the results of the formation of $HCOO^-$ (indicated by band area around 1580 cm^{-1}) at 70 °C. The $HCOO^-$ formation on CeO_2-N is slightly higher than corresponding peaks of CeO_2-P. However, for Ag/CeO_2-N catalysts, $HCOO^-$ peak intensity continues to increase, and the $HCOO^-$ intensity on the surface is significantly higher than the other three catalysts after 30 min. Accordingly, in the atmosphere of HCHO with or without O_2, the decrease ranks of the formation of $HCOO^-$ is Ag/CeO_2-N > Ag/CeO_2-P > CeO_2-N > CeO_2-P, which is the same as the sequence of the HCHO catalytic oxidation test. For the catalytic oxidation reaction to proceed at an appreciate rate, further transient study were carried out at relatively higher temperature of 100 °C. The decreasing trend of $HCOO^-$ in Fig. S3 obviously indicate that the $HCOO^-$ is the main intermediate species in the catalytic oxidation reaction of HCHO, which should be further oxidized by oxygen into the final product H_2O and CO_2. The above speculation is consistent with some previous reports of catalytic oxidation reaction of HCHO on silver catalysts [24,25].

4. Conclusion

The present work shows that Ag/CeO_2 nanosphere catalysts exhibits much higher catalytic activity than Ag/CeO_2 and pure CeO_2 particles. Ag/CeO_2 nanosphere catalysts are relatively active, and could reach approximately 100% HCHO oxidation conversion above 110 °C under relatively high space velocity. The specific reaction rate of Ag/CeO_2-N catalysts is almost 3.6 times higher than Ag/CeO_2 particle catalysts at 110 °C. Therefore, the Ag/CeO_2 nanospheres might be a promising catalyst for practical application in catalytic oxidation of formaldehyde. High-resolution transmission electron microscope shows that Ag/CeO_2 nanosphere catalysts, with average sizes around 80–100 nm, are comprised of many small particles with a crystallite size of 2–5 nm, and there are clear voids among the small particles. Meanwhile, cerium and silver well disperse throughout the individual Ag/CeO_2 nanosphere crystals. According to the results in XPS, H_2-TPR, O_2-TPD, and Raman, much more surface chemisorbed oxygen easily forms on the Ag/CeO_2 nanosphere catalysts. Synergetic interaction might exist between silver nano particles and CeO_2 nanospheres, and the presence of silver could facilitate oxygen activation, which mainly contributes to the HCHO oxidation reaction. In the catalytic oxidation process of HCHO, formate species ($HCOO^-$) are the key intermediates and are activated on the surface active oxygen of Ag/CeO_2 nanosphere catalysts, which will be further oxidized into the final product water and carbon dioxides.

Acknowledgments

This work was supported by the State Key Project of Fundamental Research for Nanoscience and Nanotechnology (2011CB932401 and 2011CBA00500), National key Basic Research Program of China (2012CB224802), and the National Natural Science Foundation of China (Grant No. 21221062, 21171105, 21322107 and 21131004). Lei Ma gratefully acknowledges the financial support provided by special fund of State Key Joint Laboratory of Environment Simulation and Pollution Control (13K04ESPCT) and China Postdoctoral Science Foundation (2013M530643).

Appendix A. Supplementary data

Supplementary data associated with this article can be found, in the online version, at http://dx.doi.org/10.1016/j.apcatb.2013.10.039.

References

[1] J. Quiroz Torres, S. Royer, J.-P. Bellat, J.-M. Giraudon, J.-F. Lamonier, ChemSusChem 6 (2013) 578–592.
[2] H. Chen, J. He, C. Zhang, H. He, Journal of Physical Chemistry C 111 (2007) 18033–18038.
[3] Y. Xia, H. Dai, L. Zhang, J. Deng, H. He, C.T. Au, Applied Catalysis B: Environmental 100 (2010) 229–237.
[4] L. Bai, F. Wyrwalski, J.-F. Lamonier, A.Y. Khodakov, E. Monflier, A. Ponchel, Applied Catalysis B: Environmental 138–139 (2013) 381–390.
[5] B. Bai, H. Arandiyan, J. Li, Applied Catalysis B: Environmental 142–143 (2013) 677–683.
[6] Y. Wang, A. Zhu, B. Chen, M. Crocker, C. Shi, Catalysis Communications 36 (2013) 52–57.
[7] C. Zhang, F. Liu, Y. Zhai, H. Ariga, N. Yi, Y. Liu, K. Asakura, M. Flytzani-Stephanopoulos, H. He, Angewandte Chemie International Edition 124 (2012) 9766–9770.
[8] S.J. Park, I. Bae, I.S. Nam, B.K. Cho, S.M. Jung, J.H. Lee, Chemical Engineering Journal 195 (2012) 392–402.
[9] B.C. Liu, Y. Liu, C.Y. Li, W.T. Hu, P. Jing, Q. Wang, J. Zhang, Applied Catalysis B: Environmental 127 (2012) 47–58.
[10] M. Jia, Y. Shen, C. Li, Z. Bao, S. Sheng, Catalysis Letters 99 (2005) 235–239.
[11] Y.N. Shen, X.Z. Yang, Y.Z. Wang, Y.B. Zhang, H.Y. Zhu, L. Gao, M.L. Jia, Applied Catalysis B: Environmental 79 (2008) 142–148.
[12] J. Zhang, Y. Jin, C. Li, Y. Shen, L. Han, Z. Hu, X. Di, Z. Liu, Applied Catalysis B: Environmental 91 (2009) 11–20.
[13] H.-F. Li, N. Zhang, P. Chen, M.-F. Luo, J.-Q. Lu, Applied Catalysis B: Environmental 110 (2011) 279–285.
[14] B.C. Liu, C.Y. Li, Y.F. Zhang, Y. Liu, W.T. Hu, Q. Wang, L. Han, J. Zhang, Applied Catalysis B: Environmental 111 (2012) 467–475.
[15] B.-B. Chen, C. Shi, M. Crocker, Y. Wang, A.-M. Zhu, Applied Catalysis B: Environmental 132–133 (2013) 245–255.
[16] C. Zhang, H. He, K.-i. Tanaka, Applied Catalysis B: Environmental 65 (2006) 37–43.
[17] X. Tang, J. Chen, X. Huang, Y. Xu, W. Shen, Applied Catalysis B: Environmental 81 (2008) 115–121.
[18] X. Tang, J. Chen, Y. Li, Y. Li, Y. Xu, W. Shen, Chemical Engineering Journal 118 (2006) 119–125.
[19] Z.P. Qu, S.J. Shen, D. Chen, Y. Wang, Journal of Molecular Catalysis A: Chemical 356 (2012) 171–177.
[20] C. Shi, B.B. Chen, X.S. Li, M. Crocker, Y. Wang, A.M. Zhu, Chemical Engineering Journal 200 (2012) 729–737.
[21] Z.W. Huang, X. Gu, Q.Q. Cao, P.P. Hu, J.M. Hao, J.H. Li, X.F. Tang, Angewandte Chemie International Edition 51 (2012) 4198–4203.
[22] D. Chen, Z. Qu, Y. Sun, K. Gao, Y. Wang, Applied Catalysis B: Environmental 142–143 (2013) 838–848.

[23] C. Sun, H. Li, L. Chen, Energy & Environmental Science 5 (2012) 8475–8505.
[24] S. Imamura, D. Uchihori, K. Utani, T. Ito, Catalysis Letters 24 (1994) 377–384.
[25] C.F. Mao, M.A. Vannice, Journal of Catalysis 154 (1995) 230–244.
[26] D. Wang, T. Xie, Y. Li, Nano Research 2 (2009) 30–46.
[27] X. Liang, J.J. Xiao, B.H. Chen, Y.D. Li, Inorganic Chemistry 49 (2010) 8188–8190.
[28] C. Ma, D. Wang, W. Xue, B. Dou, H. Wang, Z. Hao, Environmental Science and Technology 45 (2011) 3628–3634.
[29] N.H. An, W.L. Zhang, X.L. Yuan, B. Pan, G. Liu, M.J. Jia, W.F. Yan, W.X. Zhang, Chemical Engineering Journal 215 (2013) 1–6.
[30] S. Imamura, H. Yamada, K. Utani, Applied Catalysis A: General 192 (2000) 221–226.
[31] Y. Kang, M. Sun, A. Li, Catalysis Letters 142 (2012) 1498–1504.
[32] L.H. Tjeng, M.B.J. Meinders, J. van Elp, J. Ghijsen, G.A. Sawatzky, R.L. Johnson, Physical Review B: Condensed Matter 41 (1990) 3190–3199.
[33] J.F. Weaver, G.B. Hoflund, Journal of Physical Chemistry 98 (1994) 8519–8524.
[34] H. Zhang, A. Zhu, X. Wang, Y. Wang, C. Shi, Catalysis Communications 8 (2007) 612–618.
[35] Z. Wu, M. Li, J. Howe, H.M. Meyer, S.H. Overbury, Langmuir 26 (2010) 16595–16606.